2019

General π-electron-assisted strategy for single-atom (Ir, Pt, Ru, Pd, Fe, and Ni) electrocatalysts with bi-functional active sites toward highly efficient water splitting

Weihong Lai
University of Wollongong, weihongl@uow.edu.au

Li-Fu Zhang
Nankai University

Wei-Bo Hua
Karlsruhe Institute of Technology

Sylvio Indris
Karlsruhe Institute of Technology

Zichao Yan
University of Wollongong, zy820@uowmail.edu.au

See next page for additional authors

Publication Details

Lai, W., Zhang, L., Hua, W., Indris, S., Yan, Z., Hu, Z., Zhang, B., Liu, Y., Wang, L., Liu, M., Liu, R., Wang, Y., Wang, J., Hu, Z., Liu, H., Chou, S. & Dou, S. (2019). General p-Electron-Assisted Strategy for Ir, Pt, Ru, Pd, Fe, Ni Single- Atom Electrocatalysts with Bifunctional Active Sites for Highly Efficient Water Splitting. Angewandte Chemie-international Edition, 58 (34), 11868-11873.

General π-electron-assisted strategy for single-atom (Ir, Pt, Ru, Pd, Fe, and Ni) electrocatalysts with bi-functional active sites toward highly efficient water splitting

Abstract

Both the hydrogen evolution reaction (HER) and the oxygen evolution reaction (OER) are crucial to water splitting, but require alternative active sites. Now, a general pelectron- assisted strategy to anchor single-atom sites (M=Ir, Pt, Ru, Pd, Fe, Ni) on a heterogeneous support is reported. The Matoms can simultaneously anchor on two distinct domains of the hybrid support, four-fold N/C atoms (M@NC), and centers of Co octahedra (M@Co), which are expected to serve as bifunctional electrocatalysts towards the HER and the OER. The Ir catalyst exhibits the best water-splitting performance, showing a low applied potential of 1.603V to achieve 10 mAcm@2 in 1.0m KOH solution with cycling over 5 h. DFT calculations indicate that the Ir@Co (Ir) sites can accelerate the OER, while the Ir@NC3 sites are responsible for the enhanced HER, clarifying the unprecedented performance of this bifunctional catalyst towards full water splitting.

Keywords

ni, fe, pd, ru, pt, single-, ir, strategy, p-electron-assisted, general, atom, electrocatalysts, bifunctional, active, sites, highly, efficient, splitting, water

Disciplines

Engineering | Physical Sciences and Mathematics

Publication Details

Lai, W., Zhang, L., Hua, W., Indris, S., Yan, Z., Hu, Z., Zhang, B., Liu, Y., Wang, L., Liu, M., Liu, R., Wang, Y., Wang, J., Hu, Z., Liu, H., Chou, S. & Dou, S. (2019). General p-Electron-Assisted Strategy for Ir, Pt, Ru, Pd, Fe, Ni Single- Atom Electrocatalysts with Bifunctional Active Sites for Highly Efficient Water Splitting. Angewandte Chemie-international Edition, 58 (34), 11868-11873.

Authors

Weihong Lai, Li-Fu Zhang, Wei-Bo Hua, Sylvio Indris, Zichao Yan, Zhe Hu, Binwei Zhang, Yani Liu, Li Wang, Min Liu, Rong Liu, Yunxiao Wang, Jiazhao Wang, Zhenpeng Hu, Hua-Kun Liu, Shulei Chou, and Shi Xue Dou

RESEARCH ARTICLE

General π-electron-assisted strategy for single-atom (Ir, Pt, Ru, Pd, Fe, and Ni) electrocatalysts with bi-functional active sites toward highly efficient water splitting

Wei-Hong Lai, [a]1 Li-Fu Zhang, [b]1 Wei-Bo Hua,[c] Sylvio Indris,[c] Zi-chao Yan,[a] Zhe Hu,[a] Binwei Zhang,[a] Yani Liu,[d] Li Wang,[a] Min Liu,[e] Rong Liu, [f] Yun-Xiao Wang,[a] Jia-Zhao Wang,*[a] Zhenpeng Hu, [b] Hua-Kun Liu,[a] Shu-Lei Chou,*[a] Shi-Xue Dou[a]

Abstract: Both the hydrogen evolution reaction (HER) and the oxygen evolution reaction (OER) are crucial in water splitting, but demand alternative active sites. It is challenging to build dual catalytic abilities on one catalyst with efficient, stable, cheap characteristics, simultaneously promoting both the HER and the OER. Here, we report a general π-electron-assisted strategy to anchor diverse single-atom sites (M_1), including iridium (Ir_1), platinum (Pt_1), ruthenium (Ru_1), palladium (Pd_1), iron (Fe_1), and nickel (Ni_1), on a heterogeneous support. It is remarkable that the M1 atoms can simultaneously anchor on two distinct domains of the hybrid support, four-fold N/C atoms (M_1@NC) and centers of Co octahedra (M_1@Co), which are expected to serve as bifunctional electrocatalysts towards the HER and the OER, respectively. Among them, the catalyst Ir_1 exhibits the best water splitting performance, showing a low applied potential of 1.603 V to achieve 10 mA cm^{-2} in 1.0 M KOH solution with cycling over 5 h. The density functional theory calculations indicate that the Ir_1@Co (Ir) sites can accelerate the OER, while the $Ir_1@NC_3$ sites are responsible for the enhanced HER, clarifying the unprecedented performance of this bi-functional catalyst towards full water splitting.

Introduction

Single-atom catalysts (SACs) hold great promise for maximizing the catalytic efficiency of supported metals by achieving the ultimate utilization of every single atom.[1, 2] Multifarious single atoms have been fabricated and demonstrated their ultimate size effects, such as Co_1,[3] Pt_1[4], Ru_1[5], Ir_1[6], Fe_1[7], and Pd_1[4d, 8]. Significantly, various SACs show remarkable catalytic activity and selectivity toward a variety of electrocatalytic reactions, including the hydrogen evolution reaction (HER)[4f], the oxygen evolution reaction (OER)[9], the oxygen reduction reaction (ORR)[4c, 5a], the CO oxidation reaction[4a, 4g, 10], the CO_2 reduction reaction [4d], the water gas shift reaction[6], and hydrogenation[8b] with high efficiency. It is noteworthy that the same foreign isolated substitutions can be tuned to show distinct catalytic activities *via* anchoring on different supports. For instance, Yang *et al*. achieved greatly different activity of a single-atom Pt catalyst on two supports, titanium carbide and titanium nitride, towards the ORR; the oxygen reduction current density of Pt_1/TiC was almost two times larger than that of Pt_1/TiN in all potential ranges, suggesting higher selectivity towards producing H_2O_2 [11]. It is believed that the strong metal support interactions (SMSI) can change the physics of the orbitals, band gap, electron density, and surface chemistry of the SACs, so that they exhibit different catalytic properties for a wide variety of chemical reactions. On the other hand, electrochemical water splitting is regarded as the most efficient and clean technology for high-purity hydrogen generation. It can be utilized to convert intermittent sources of renewable energy such as solar and wind into chemical energy stored by hydrogen fuel.[12] The overall water splitting involves active electrocatalysis towards the anodic OER and the cathodic HER. Bimetallic transition metal surface can tune the absorption energy via changing the filling level on d-bands, showing superior performance towards the OER, while metal doped carbon-based catalysts exhibits high activity towards the HER.[13] It is thus ideal to construct an efficient bi-functional catalyst with synergistic dual active sites, including transition metal surface and carbon matrix, that can simultaneously promote both the HER and the OER.

Herein, zeolitic imidazolate framework-67 (ZIF-67) is selected as an ideal precursor to fabricate diverse bi-functional SACs. It possesses unique π-electrons in the imidazole pentagons that can act as aggregation inhibitors, which initially bond with metal ions *via* strong π conjunction, thus successfully stabilizing the single metal atom species. Moreover, the ZIF-67 can be transformed into a heterogeneous support with Co nanoparticles dispersed in N-doped porous carbon (Co/NC). This unique Co/NC support provides two distinct domains for generally anchoring various single metal ions (M_1= Ir_1, Pt_1, Pd_1, Ru_1, Fe_1, and Ni_1), leading to the formation of a series of M_1@Co/NC catalysts. As shown in Figure 1a, in a M_1@Co/NC catalyst, both Co and NC can serve as substrates for single atoms, respectively, which subsequently corresponds to two different active sites, M_1@Co and M_1@NC, simultaneously accelerating the OER and the HER. Moreover, the M_1@Co/NC catalysts demonstrate unique three dimensional (3D) isolated atomic dispersion of various metals by virtue of the distinctive tunneling effects of the ZIF-67 structure. Significantly, the obtained Ir_1@Co/NC catalyst displays the highest activity toward overall water splitting, achieving an applied potential of 1.603 V vs. reversible hydrogen electrode (RHE) with current density of 10 mA cm^{-2} in 1.0 M KOH solution. The catalytic activities are further clarified by the density functional theory (DFT) calculations, which indicate that the $IrNC_3$ sites are responsible for the efficient HER capability while the Ir@CoO (Ir) sites are beneficial for the OER.

Results and Discussion

[a] Institute for Superconducting & Electronic Materials, University of Wollongong, Innovation Campus, Wollongong, NSW 2500, Australia.
[b] School of Physics, Nankai University, Tianjin 300071, China.
[c] Institute for Applied Materials (IAM), Karlsruhe Institute of Technology (KIT), Hermann-von-Helmholtz-Platz 1, 76344 Eggenstein-Leopoldshafen, Germany.
[d] BUAA-UOW Joint Centre, School of Physics, Beihang University, Beijing 100191, China
[e] College of Material and Science, Beijing University of Technology, Beijing 100124, China.
[f] SIMS Facility, Western Sydney University, Locked Bag 1797, Penrith, NSW 2751, Australia
Supporting information for this article is given via a link at the end of the document.((Please delete this text if not appropriate))

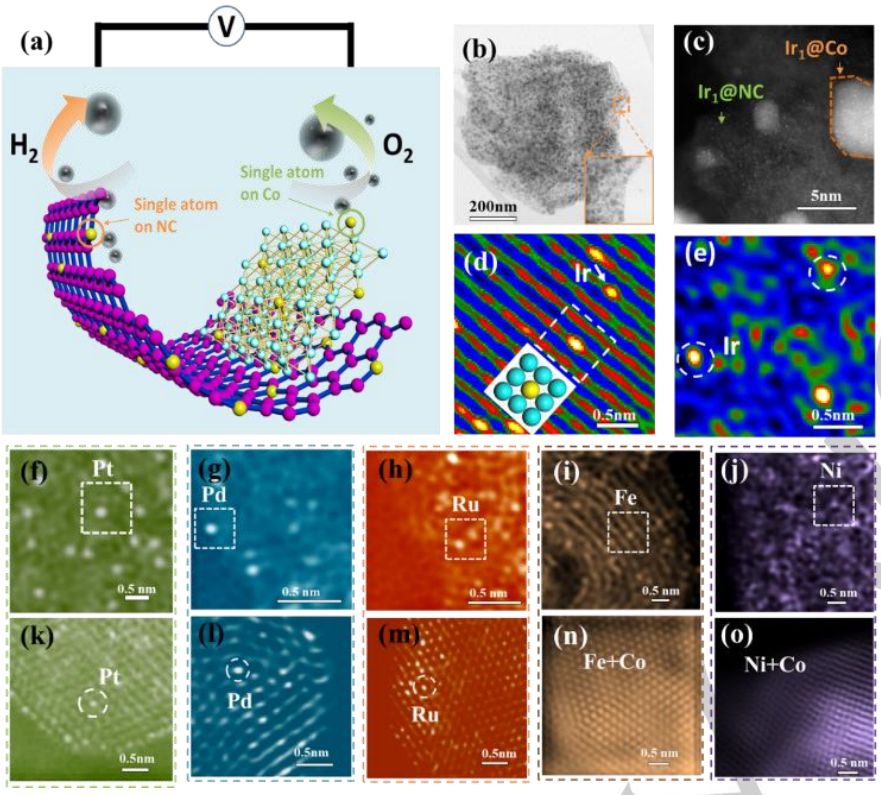

Figure 1. (a) Schematic illustration of the working mechanism of the prepared electrodes. (b) Annular bright field (ABF)-STEM images of Ir_1@Co/NC at low magnification. (c) HAADF-STEM image of Ir_1@Co/NC at high magnification. (d) HAADF-STEM image of Ir_1@Co region, (e) FFTI-HAADF image of Ir_1@NC area. FFTI-HAADF images of (f) Pt_1, (g) Pd_1, (h) Ru_1, (i) Fe_1, and (j) Ni_1 on NC (above) and their corresponding FFTI-HAADF images on Co particles (below).

As illustrated in Figure S1 in the Supporting Information, when various metal cations (M^{2+}, M= Ir/Pt/ Pd/Ru/Fe/Ni) are added into the ZIF-67 dispersion, a series of ZIF-67-M mixtures can be formed via strong coordination of M^{2+} with imidazole pentagons via electron absorption under continual stirring. During pyrolysis at 600-700 °C under Ar atmosphere, ZIF-67 precursor is transformed into the heterogeneous Co/NC support; simultaneously, the coordinated M^{2+} ions are reduced into metal single atoms (M_1) through the carbonization of the organic linkers, leading to the formation of isolated M_1 embedded in the Co and NC domains of the support (M_1@Co/NC). The high angle annular dark field (HAADF)-scanning transmission electron microscopy (STEM) image at low magnification shows that the representative Ir_1@Co/NC (2.2 wt% Ir, as confirmed by inductively coupled plasma – optical emission spectrometry (ICP-AES)) exhibits a roughly dodecahedral shape without any particles with striking contrast observed on the surface (Figure 1b). The high-magnification HAADF image of the Ir_1@Co/NC verifies that high-density Ir single atoms are uniformly dispersed on both Co nanoparticles and the C matrix without agglomeration during the high-temperature annealing process of the ZIF-67-Ir mixture (Figure 1c).The intensity mapping of the high-resolution HAADF image in Fig. 1d demonstrates the highly contrast in electronic intensity of the different atoms, that is, the high energy atoms correspond to the red-color dot, and the low energy atoms show a gradient change to the blue color. The red dots correspond to the isolated Ir single atoms on the Co nanoparticles, which evidently occupy the positions of Co atoms, as illustrated in the white box. Hence, this portion of Ir_1 is stabilized by alloying with Co atoms to form single atom alloys (SAAs). It is believed that the alloyed Ir_1@Co SAAs can exhibit geometric and electronic structures different from those of the single atoms that are prepared by anchoring on the support. [8c, 14] Thus, the Ir_1@Co are expected to show a low energy barrier, and high selectivity and activity in catalytic reactions.[15] Furthermore, the fast Fourier transform inverse high resolution HAADF (FFTI-HAADF) image clearly shows a high-density of bright isolated Ir atoms dispersed on the carbon layer (Figure 1e). More importantly, this synthetic strategy can be generalized to various metals, including Pt, Pd, Ru, Fe, and Ni, based on the abovementioned Co-alloying and N-coordination interactions. The bright contrast single atoms of Pt (2.28 wt%, Pt_1@Co/NC), Pd (1.9 wt%, Pd_1@Co/NC), Ru (2.0 wt%, Ru_1@Co/NC), Ni (1.8 wt%, Ni_1@Co/NC), and Fe (1.3 wt%, Fe_1@Co/NC) are uniformly dispersed on the Co/NC support without any observable particles (Figure S2). Moreover, as shown in Figure 1f-j, the high resolution HAADF images show that single atoms of Pt, Pd, Ru, Fe, and Ni are isolated in the nitrogen-doped carbon matrix (white rectangle), indicating the very strong coordination effect between C/N groups and metal ions. Also, as shown in the images below (Figure 1k-o), these single atoms of Pt_1, Pd_1, Ru_1, Fe_1, and Ni_1, in a similar way to Ir_1, are successfully doped on Co crystal without agglomeration. The STEM-energy dispersive spectroscopy (EDS) element mapping further confirmed that the expected elements Ir, C, N, and Co were uniformly distributed over the entire architecture (Figure S3). The regional EDS analysis on Ir_1@Co/NC shows that the Ir_1 single atoms have a higher mass ratio on carbon than that on carbon matrix (Figure S4). Similarly, the other single atoms (Pt_1/Pd_1/Ru_1/Fe_1/Ni_1) were uniformly dispersed in the substrate (Co/NC) (Figures S5-S9).

Furthermore, the X-ray diffraction patterns (XRD) of all M_1@Co/NC samples are well consistent with the Co/NC, only showing three peaks at 44.2°, 51.5°, and 75.9°, which are indexed to the (111), (200), and (202) planes of Co (Figure S10), respectively. No other metal phases are formed in these M_1@Co/NC samples, further implying that the loaded metals are very likely to be atomically dispersed in the support without

forming nanoclusters/nanoparticles with M-M stacking. In addition, thermogravimetric analysis (TGA) indicates that the mass ratios of Co and C in the Co/NC support are 65% and 35%, respectively (Figure S11).

The electrochemically catalyzed HER and OER with the M_1@Co/NC were evaluated in N_2-saturated 1.0 M KOH solutions *via* a typical three-electrode cell at room temperature. The linear sweep voltammetry (LSV) curves of the Ir_1@Co/NC, Pt_1@Co/NC, Pd_1@Co/NC, Ru_1@Co/NC, Ni_1@Co/NC, and Fe_1@Co/NC electrodes are shown in Figure 2a with a scan rate of 10 mV s^{-1} for HER. It is evident that both Ir_1@Co/NC show the most positive onset potential with an overpotential of 55 mV, and the Ir_1@Co/NC electrode in particular exhibits a similar polarization curve to commercial Pt/C, which requires 0.06 V to deliver 10 mA cm^{-2} current density. Notably, the over-potentials (η) involved in achieving a 10 mA cm^{-2} current density increase in the sequence: Fe_1@Co/NC < Pd_1@Co/NC < Pt_1@Co/NC < Ni_1@Co/NC < Ru_1@Co/NC < Ir_1@Co/NC, indicating that the Ir_1@Co/NC achieves the best HER performance. The Tafel plots as shown in Figure 2b, which are derived from the polarization curves (Figure 2a), indicate that the electrode of Ir_1@Co/NC (119 mV dec^{-1}) has the lowest Tafel slope compared with Ru_1@Co/NC (210 mV dec^{-1}), Fe_1@Co/NC (310 mV dec^{-1}), Pd_1@Co/NC (133 mV dec^{-1}), Pt_1@Co/NC (151 mV dec^{-1}), and Ni_1@Co/NC (253 mV dec^{-1}). In particular, the Ir_1@Co/NC catalyst shows a comparable Tafel slope to Pt/C (79 mV dec^{-1}), suggesting favorable HER kinetics via a Volmer-Heyrovsky pathway.

On the other hand, the polarization curves shown in Figure 2c revealed that the Ir_1@Co/NC presented superior OER catalytic activity. The over-potentials delivering a current density of 10 mA cm^{-2} are in the followed sequence: Ir_1@Co/NC (260 mV) > IrO_2 (385 mV) > Ni_1@Co/NC (370 mV) > Pt_1@Co/NC (430 mV) > Pd_1@Co/NC (470 mV) = Ru_1@Co/NC (470 mV) > Fe_1@Co/NC (500 mV). Also, Ir_1@Co/NC shows a Tafel slope of 163 mV dec^{-1}, which is better than those of Ni_1@Co/NC (222 mV dec^{-1}), and Fe_1@Co/NC (330 mV dec^{-1}), indicating that Ir_1@Co/NC has better OER kinetics due to a possibly high exchange current density (Figure 2d). The Pt_1@Co/NC (124 mV dec^{-1}), Ru_1@Co/NC (140 mV dec^{-1}), and Pd_1@Co/NC (125 mV dec^{-1}), however, presented a faster exchange current, which is near that of the commercial IrO_2. As summarized in Figure 2e, the overall over-potentials of the HER and OER indicate that Ir_1@Co/NC

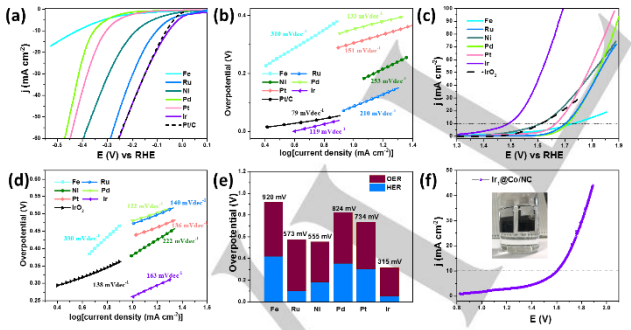

Figure 2. (a, c) Polarization curves of the HER and the OER of Ir_1@Co/NC, Pt_1@Co/NC, Pd_1@Co/NC, Ru_1@Co/NC, Ni_1@Co/NC, Fe_1@Co/NC, and commercial Pt/C and IrO_2 electrodes. (b, d) The corresponding Tafel slopes obtained from the polarization curves (a, c), respectively. (e) The overall over-potential of the corresponding electrodes obtained at 10 mA cm^{-2}. (f) The polarization curves of overall water splitting by the Ir_1@Co/NC catalyst. Inset is the image of a two electrode system which is producing bubbles of H_2 and O_2 at an applied potential of 1.4 V (vs. RHE).

(315 mV) had a lower over-potential than these other electrodes (Fe_1@Co/NC (920 mV), Ni_1@Co/NC (555 mV)), Pt_1@Co/NC (734 mV), Pd_1@Co/NC (824 mV), and Ru_1@Co/NC (573 mV)), suggesting that Ir_1@Co/NC is a highly efficient bi-functional catalyst that can achieve excellent performance with an low overall potential window in water splitting. Accordingly, we integrated two Ir_1@Co/NC electrodes loaded on carbon paper (1.2 cm × 1 cm) as water electrolysis anode and cathode in 1.0 M KOH electrolyte solution. It is clearly observed that the hydrogen and oxygen bubbles are formed when the applied potential is higher than 1.4 V (inset image, Figure 2f). Also, the current density of 10 mA cm^{-2} can be achieved with a potential of 1.603 V, which is consistent with the supposed potential window. It is highly significant that the Ir_1@Co/NC catalyst can facilitate stable long-term overall water splitting over the course of 5 h with a set potential of 1.61 V via constant voltage electrolysis (Figure S12). A comparison of the overpotentials and mass activities of reported overall water-splitting catalysts based on noble metals indicates that Ir_1@Co/NC shows overwhelming mass activity with a comparable overall potential at current density of 10 mA cm^{-2}, regardless whether the electrolyte is acidic or basic (Table S1, Supporting Information).

The adsorption properties on H, and O are primarily depend on surface chemistry and electronic structures, which in turn is determined its geometric structure and chemical bonding[16]. In this work, the focused ion beam scanning electron microscopy (FIB-SEM), X-ray adsorption spectrum (XAS), and secondary ion mass spectroscopy (SIMS) as well as the DFT calculations have been utilized to investigate the specific active surface, bonding environments, and electronic structure of single atoms. The FIB-SEM and SIMS results confirm that the single metal atoms are 3D isolated atomic dispersion over the surface and cross-section on both carbon matrix and Co (Figure S13-S16). The 3D dispersion of single atoms is conducive to the exposure of more active sites for water splitting, which is ascribed to the easy accessibility of the zeolitic structure and the numerous functional organic groups anchored on each tunnel.

DFT calculations were performed to elucidate the electrocatalytic mechanism of the Ir_1@Co/NC towards its accelerated HER and OER. The local structure of Ir_1 on Co/NC is confirmed via the EXAFS fitting, which forms a complex with four-fold N/C atoms on a porous carbon matrix and are alloyed in the centers of Co octahedra (Figure S17). Additionally, the XPS results suggest that the atomic ratio of C to N is around 4.82 (Figure S18), which means that $IrNC_3$ and IrC_4 are the most probable model for a four-fold coordination structure, as shown in Figure 3a-b. Additionally, it is well known that an oxidation layer would be easily generated on the Co surface, forming CoO layers at the applied potential of the OER, which is typically higher than 1.23 V (vs. RHE).[17] Thus, the adsorption energies of oxygen-based intermediates on the (100) surface of CoO were calculated as well, in which a Co atom on the surface is replaced by an Ir atom (denoted as Ir_1@CoO), as shown in Figure 3c and d. It is ideal that the free energy of H* adsorption for a good HER catalyst should be close to zero, which is beneficial for both adsorption of H* and desorption of H_2. The optimized geometries of the adsorption structures of H* intermediates on $IrNC_3$, IrC_4, Ir_1@Co (Co), and Ir_1@Co (Ir) models are shown in Figure S19. Figure 3e shows the free energy changes with H* adsorption (ΔG_{H^*}) for the Ir_1@Co on $IrNC_3$, IrC_4, Ir_1@Co (Co), and Ir_1@Co (Ir), respectively. Two possible H* adsorption configurations on the Co site (0.48 eV) and Ir (0.68 eV) site show large positive values and are far away from the neutral position, indicating that the Ir_1@Co has a high barrier for the rate determining step in alkaline solution. In comparison, single atom Ir_1 on a four-fold carbon structure (IrC_4 (0.46 eV), $IrNC_3$ (-0.39 eV)) is favorable to the adsorption and dissociation of water molecules, showing a smaller ΔG_{H^*}.

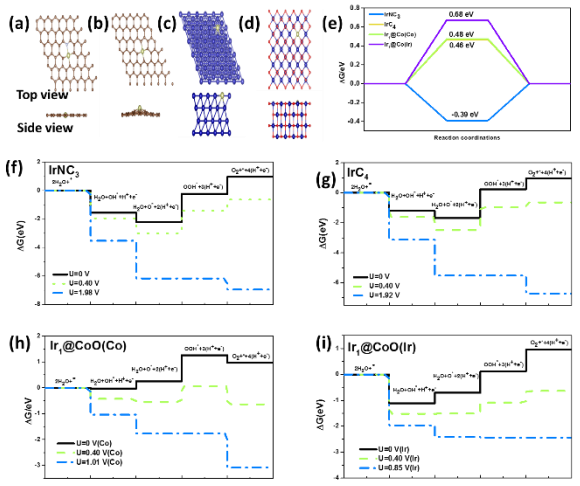

Figure 3. (a, b, c, d)Top views and side views of $IrNC_3$, IrC_4, Ir@Co, and Ir@CoO, respectivelygray, white, yellow, blue, and red balls represent C, N, Ir, Co, and O atoms. (e) The free energy diagrams for the HER at pH = 14 on $IrNC_3$, IrC_4, Ir_1@Co (Co), and Ir_1@Co (Ir). The reaction free energies of the intermediates on (f) $IrNC_3$, (g) IrC_4, (h) Ir_1@CoO(Co), and (i) Ir_1@CoO(Ir). (n) Density of states of samples at pH = 14.

The OER performance was also computed on the four possible catalytic sites, and the free energies of their intermediates are plotted at pH = 14, showing the different values applied at different potential *U* values (Figure S20). It is well known that four elementary steps are involved in producing O_2, as shown in Figure 3f-i. A variety of over-potentials (η) were applied to decrease the rise in free energy obtained at the equilibrium potential (U = 0.40 V). In particular, the over-potential needed is 1.58 V (Figure 3f), 1.52 V (Figure 3g), 0.61 V (Figure 3h), and 0.45 V (Figure 3i) for $IrNC_3$, IrC_4, Ir_1@CoO (Co), and Ir_1@CoO (Ir), respectively, indicating that the structure consisting of single atom Ir on a Co particle is the most efficient catalytic site for generating oxygen (Figure S20). Significantly, the same free energy ΔG_{H^*} of the fourth and final step (Figure 3i) means that the Ir_1@CoO (Ir) can go straight to producing OOH* and O_2 without any further decrease in free energy ΔG_{H^*}. The computational calculations confirmed that the single atom Ir located on the heterogeneous substrate can facilitate the transformation from H_2O molecules to H_2 and O_2 in alkaline solution, thus simultaneously promoting the OER (Ir_1@CoO (Ir)) and HER (Ir_1@NC_3). Also, as illustrated by the projected density of states (PDOS) in Figure S21, the free atoms Ir_1 doped on both NC and CoO show higher and narrower occupied states, which are mostly contributed by their *d* orbitals near Fermi level. This reveals that the single atom Ir_1 can effectively improve the *d*-electron dominance near the Fermi level and promote electron transfer, leading to higher conductivity and enhanced catalytic activity as well.[17a] In order to experimentally verify the activity differences of Ir_1 anchored on distinct substrates, a control sample Ir_1@NC has been prepared (Figure S22). In contrast to Ir_1@Co/NC, the Ir_1@NC shows a minor decrease of the overpotential for HER but a serious fading towards OER (Figure S23), confirming that the Ir single atom on carbon matrix is mainly responsible for the high HER performance and the Co component in the support can also assist in improving the HER ability due to the enhanced conductivity. This results are well consistent with our experimental reulsts and DFT calculations.

It, thus, is of significance to investigate the mechanism of the general strategy to synthesize 3D-dispersed single atoms, including precious metal elements and transition elements, on the heterogeneous support, which can lead to dual active sites with different electronic properties towards different catalytic reactions. DFT calculations were performed to evaluate the favorable sites (N sites, Co sites, and C sites) on ZIF-67 for metal adsorption, including Pt, Pd, Ir, Ru, Fe, and Ni (Figure 4a). The calculated adsorption energies of metals at different sites are presented in Table S2, indicating the metal atom prefer to adsorb on the imidazole ring. Particularly, due to the fact that the electronegativity of N is higher than that of C, the electron will be polarized to N atoms more than C atoms. The deformation charge density also demonstrated that both C-C and C-N bonds can cause charge redistribution of all five atoms in the pentagon rings (Figure 4b). This indicates that conjugated π bond exist in such pentagonal C-N substructures of ZIF-67, which is consistent with the electron energy loss spectroscopy (EELS) spectrum result (Figure S24). For more specifically illustrating the interaction between the metal atom and imidazole pentagonal, the metal cation Pt^{2+} were used as example. For instance, the ultraviolet–visible (UV−vis) spectrum of ZIF-67-Pt (Pt^{2+} adsorbed on ZIF-67) shows a slight blue-shift of the λ_{max} (582 → 579 nm), while a slight red-shift is observed in the mid-gap transition (303 → 308 nm) and π transition, suggesting the *p*-type nature of its doping (Figure S25).[18] The evolution of Pt_1@Co/NC with temperature was monitored from room temperature (RT) to 600 ºC.

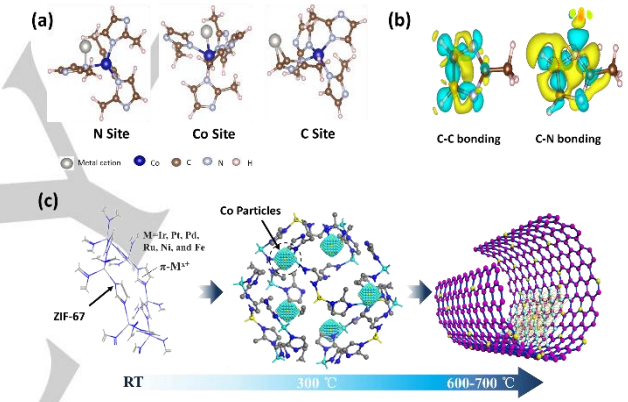

Figure 4. (a) Atomic configurations of three adsorption sites: the N site; Co site; and C site. (b) Calculated charge redistribution of C-C bond and C-N bond in ZIF-67. The two atoms calculated in the bonds are denoted by red circles. The yellow and blue isosurface indicates gain or loss of electron density due to bond formation. (c) Schematic illustration of the correlation between metal cation and π electrons. The metal cations were initially correlated with π electrons at room temperature; with the temperature increased, the metal atom embedded on cobalt forming single atom on Co at 300 °C and carbon matrix at 600-700 °C.

The K^3-weighted Fourier transform (FT) spectra from extended X-ray absorption fine structure (EXAFS) of these samples were obtained at different temperatures (Figure S26), which indicates that the Pt^{2+} ions are bonded with low coordination numbers (purple dashed line) below 600 ℃ and form Pt-Co bonds with high coordination numbers in a long R-space (green dashed line) from 300 to 600 ℃, which is consistent with the STEM result (Figure S27). The (EXAFS) fitting curve of the ZIF-67-Pt mixture suggests that the Pt_1 atoms are sitting on top of the pentagonal ring and binding with five nitrogen/carbon atoms (Figure S28). The FFTI-HAADF image and color mapping of the ZIF-67-Pt mixture at 25 ℃ also shows clear evidence that the bright contrast Pt ions were trapped on the edges of the pentagons of 2-methylimidazole (Figure S29), indicating that Pt ions are initially anchored in the imidazole groups before the thermal treatment. In particular, a control sample (Co/NC) to compare. Due to the absence of imidazole groups in the Co/NC substrate, the mixed Pt ions were severely aggregated and formed Pt particles, but no isolated single atoms were dispersed after annealing (Figure S30), implying that the imidazole groups of ZIF-67 play a key role in preparing single atoms. Thus, these results indicate that the

delocalized π electrons in imidazole groups are the most critical for single atoms, which serve as anchoring sites to initially form strong bonding with the M ions and keep them isolated through the thermal carbonization (Figure 4c).

Conclusion

In sum, through coordinating with the π electrons on imidazole group of ZIF-67, the bonding of metal ions (Pt^{2+}/Ir^{2+}/Pd^{2+}/Ru^{2+}/Ni^{2+}/Fe^{2+}) can cause them to be stabilized as isolated single atoms anchored on the heterogeneous substrate, composed of a nitrogen doped carbon matrix and cobalt nanoparticles, via a facile pyrolysis process. The formation mechanism and high reactivity of these atomically dispersed atoms were systematically explored by control experiments and DFT calculations. The high accessibility of numerous tunnels on ZIF-67 frameworks leads to the unique 3D dispersion of single atoms, thus achieving an ultrahigh density of active sites. Such fascinating structures for these highly active materials, such as Ir_1@Co/NC, enable them to act as superior catalysts on reaction electrodes for the HER and OER. DFT calculations enabled us to build a variety of possible Ir_1 active sites, showing that Ir_1@CoO (Ir) is responsible for the high OER performance, while $Ir_1@NC_3$ leads to the superior HER efficiency. Such a synergistic structure simultaneously endows this composite with an efficient and stable capability towards overall water splitting. This work sheds light on the synthesis of various single-atom catalysts with high-efficiency and multifold active sites.

Experimental Section

Experimental Details. In a typical synthesis, 100 mg ZIF-67 powders were mixed with 50 ml ethanol by ultra-sonification for 30 min to form a homogeneous dispersion. 0.0075 mmol metal salts were then added into the dispersion, with rigorously stirring until the ethanol evaporated out, forming ZIF-67-Pt/Ir/Pd/Ru/Fe/Ni mixtures, respectively. Finally, the mixtures were annealed at 600 °C (Pt/Ir/Pd/Ru)/700 °C (Fe/Ni) under argon for 2 h. These resultant products were denoted as (Pt/Ir/Pd/Ru/Fe/Ni)1@Co/CN, respectively.

Acknowledgements ((optional))

W.H. L and L.F. Z equally contributed this work. This work is financially supported by the Australian Research Council (ARC) (LP120200432, DE170100928 and DP140104062). We thank the UOW Electron Microscopy Centre for use of the facilities (LE0882813 and LE0237478). We also thank Dr. Tania Silver for critical reading of the manuscript.

Keywords: Single atom • Dual domains • Bi-functional active sites • Water splitting

[1] aA. T. Bell, Science 2003, 299, 1688-1691; bX.-F. Yang, A. Wang, B. Qiao, J. Li, J. Liu, T. Zhang, Accounts of chemical research 2013, 46, 1740-1748.

[2] aL. Zhang, L. T. Roling, X. Wang, M. Vara, M. Chi, J. Liu, S.-I. Choi, J. Park, J. A. Herron, Z. Xie, Science 2015, 349, 412-416; bC. Zhu, S. Fu, Q. Shi, D. Du, Y. Lin, Angewandte Chemie International Edition 2017; cM. Dhiman, V. Polshettiwar, ChemCatChem 2018, 10, 881-906; dY. T. Kim, K. Ohshima, K. Higashimine, T. Uruga, M. Takata, H. Suematsu, T. Mitani, Angewandte Chemie 2006, 118, 421-425.

[3] Y. J. Sa, S. O. Park, G. Y. Jung, T. J. Shin, H. Y. Jeong, S. K. Kwak, S. H. Joo, ACS Catalysis 2018, 9, 83-97.

[4] aB. Qiao, A. Wang, X. Yang, L. F. Allard, Z. Jiang, Y. Cui, J. Liu, J. Li, T. Zhang, Nature chemistry 2011, 3, 634; bB. Zhang, H. Asakura, J. Zhang, J. Zhang, S. De, N. Yan, Angewandte Chemie International Edition 2016, 55, 8319-8323; cJ. Liu, M. Jiao, L. Lu, H. M. Barkholtz, Y. Li, Y. Wang, L. Jiang, Z. Wu, D.-j. Liu, L. Zhuang, Nature communications 2017, 8, 15938; dG. Gao, Y. Jiao, E. R. Waclawik, A. Du, Journal of the American Chemical Society 2016, 138, 6292-6297; eJ. Jones, H. Xiong, A. T. DeLaRiva, E. J. Peterson, H. Pham, S. R. Challa, G. Qi, S. Oh, M. H. Wiebenga, X. I. P. Hernández, Science 2016, 353, 150-154; fX. Li, W. Bi, L. Zhang, S. Tao, W. Chu, Q. Zhang, Y. Luo, C. Wu, Y. Xie, Advanced Materials 2016, 28, 2427-2431; gM. Moses-DeBusk, M. Yoon, L. F. Allard, D. R. Mullins, Z. Wu, X. Yang, G. Veith, G. M. Stocks, C. K. Narula, Journal of the American Chemical Society 2013, 135, 12634-12645; hF. Dvořák, M. F. Camellone, A. Tovt, N.-D. Tran, F. R. Negreiros, M. Vorokhta, T. Skála, I. Matolínová, J. Mysliveček, V. Matolín, Nature communications 2016, 7, 10801.

[5] aC. Zhang, J. Sha, H. Fei, M. Liu, S. Yazdi, J. Zhang, Q. Zhong, X. Zou, N. Zhao, H. Yu, ACS nano 2017, 11, 6930-6941; bX. Wang, W. Chen, L. Zhang, T. Yao, W. Liu, Y. Lin, H. Ju, J. Dong, L. Zheng, W. Yan, Journal of the American Chemical Society 2017, 139, 9419-9422.

[6] J. Lin, A. Wang, B. Qiao, X. Liu, X. Yang, X. Wang, J. Liang, J. Li, J. Liu, T. Zhang, Journal of the American Chemical Society 2013, 135, 15314-15317.

[7] aY. Chen, S. Ji, Y. Wang, J. Dong, W. Chen, Z. Li, R. Shen, L. Zheng, Z. Zhuang, D. Wang, Angewandte Chemie International Edition 2017, 56, 6937-6941; bH. Zhang, S. Hwang, M. Wang, Z. Feng, S. Karakalos, L. Luo, Z. Qiao, X. Xie, C. Wang, D. Su, Journal of the American Chemical Society 2017, 139, 14143-14149.

[8] aE. Antolini, Energy & Environmental Science 2009, 2, 915-931; bG. Vilé, D. Albani, M. Nachtegaal, Z. Chen, D. Dontsova, M. Antonietti, N. López, J. Pérez - Ramírez, Angewandte Chemie International Edition 2015, 54, 11265-11269; cG. Kyriakou, M. B. Boucher, A. D. Jewell, E. A. Lewis, T. J. Lawton, A. E. Baber, H. L. Tierney, M. Flytzani-Stephanopoulos, E. C. H. Sykes, Science 2012, 335, 1209-1212; dH. Yan, H. Cheng, H. Yi, Y. Lin, T. Yao, C. Wang, J. Li, S. Wei, J. Lu, Journal of the American Chemical Society 2015, 137, 10484-10487.

[9] aX. Li, P. Cui, W. Zhong, J. Li, X. Wang, Z. Wang, J. Jiang, Chemical Communications 2016, 52, 13233-13236; bY. Zheng, Y. Jiao, Y. Zhu, Q. Cai, A. Vasileff, L. H. Li, Y. Han, Y. Chen, S.-Z. Qiao, Journal of the American Chemical Society 2017, 139, 3336-3339.

[10] F. Li, Y. Li, X. C. Zeng, Z. Chen, ACS Catalysis 2014, 5, 544-552.

[11] S. Yang, Y. J. Tak, J. Kim, A. Soon, H. Lee, ACS Catalysis 2017, 7, 1301-1307.

[12] aD. G. Nocera, Accounts of chemical research 2012, 45, 767-776; bJ. A. Turner, Science 2004, 305, 972-974.

[13] aY. Lee, J. Suntivich, K. J. May, E. E. Perry, Y. Shao-Horn, The journal of physical chemistry letters 2012, 3, 399-404; bJ. Tian, Q. Liu, A. M. Asiri, X. Sun, Journal of the American Chemical Society 2014, 136, 7587-7590; cJ. Kitchin, J. K. Nørskov, M. Barteau, J. Chen, The Journal of chemical physics 2004, 120, 10240-10246.

[14] aF. R. Lucci, J. Liu, M. D. Marcinkowski, M. Yang, L. F. Allard, M. Flytzani-Stephanopoulos, E. C. H. Sykes, Nature communications 2015, 6, 8550; bG. X. Pei, X. Y. Liu, X. Yang, L. Zhang, A. Wang, L. Li, H. Wang, X. Wang, T. Zhang, ACS Catalysis 2017, 7, 1491-1500.

[15] L. Bu, S. Guo, X. Zhang, X. Shen, D. Su, G. Lu, X. Zhu, J. Yao, J. Guo, X. Huang, Nature communications 2016, 7, 11850.

[16] B. Hammer, J. Nørskov, Surface Science 1995, 343, 211-220.

[17] aJ. Feng, F. Lv, W. Zhang, P. Li, K. Wang, C. Yang, B. Wang, Y. Yang, J. Zhou, F. Lin, Advanced Materials 2017, 29, 1703798; bT. Reier, Z. Pawolek, S. Cherevko, M. Bruns, T. Jones, D. Teschner, S. r. Selve, A. Bergmann, H. N. Nong, R. Schlo¨gl, Journal of the American Chemical Society 2015, 137, 13031-13040; cC. H. Chen, S. F. Abbas, A. Morey, S. Sithambaram, L. P. Xu, H. F. Garces, W. A. Hines, S. L. Suib, Advanced Materials 2008, 20, 1205-1209.

[18] aD. Zheng, X.-A. Yuan, H. Ma, X. Li, X. Wang, Z. Liu, J. Ma, Royal Society open science 2018, 5, 171928; bH. Ullah, A.-u.-H. A. Shah, S. Bilal, K. Ayub, The Journal of Physical Chemistry C 2014, 118, 17819-17830.

Entry for the Table of Contents (Please choose one layout)

Layout 1:

RESEARCH ARTICLE

Text for Table of Contents

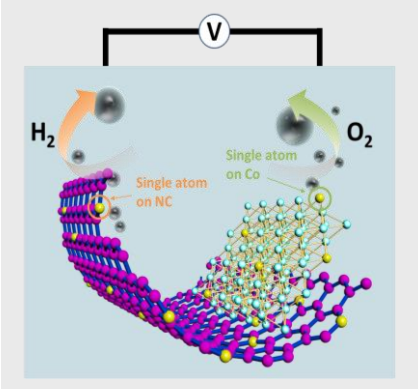

Wei-Hong Lai,[a]1 Li-Fu Zhang,[b]1 Wei-Bo Hua,[c] Sylvio Indris,[c] Zi-chao Yan,[a] Zhe Hu,[a] Binwei Zhang,[a] Yani Liu,[d] Li Wang,[a] Min Liu,[e] Rong Liu,[f] Yun-Xiao Wang,[a] Jia-Zhao Wang,[a] Zhenpeng Hu,[b] Hua-Kun Liu,[a] Shu-Lei Chou,*[a] Shi-Xue Dou[a]*

Page No. – Page No.

Title: General π-electron-assisted strategy for constructing transition metal single-atom (Ir_1, Pt_1, Ru_1, Pd_1, Fe_1, and Ni_1) electrocatalysts with bi-functional active sites toward highly efficient water splitting